

# Lean-Burn Combustor Simulator for an Engine-Component Test Facility: An Experimental and Computational Study

**Jonas Amend**

Department of Engineering Science,  
University of Oxford,  
Parks Road,  
Oxford OX1 3PJ, UK  
e-mail: jonas.amend@eng.ox.ac.uk

**Roderick Lubbock**

Department of Engineering Science,  
University of Oxford,  
Parks Road,  
Oxford OX1 3PJ, UK  
e-mail: roderick.lubbock@eng.ox.ac.uk

**Francesco Ornano**

Department of Engineering Science,  
University of Oxford,  
Parks Road,  
Oxford OX1 3PJ, UK  
e-mail: francesco.ornano@eng.ox.ac.uk

**Thomas Povey<sup>1</sup>**

Department of Engineering Science,  
University of Oxford,  
Parks Road,  
Oxford OX1 3PJ, UK  
e-mail: thomas.povey@eng.ox.ac.uk

*The computational and experimental assessment of a lean-burn low- $\text{NO}_x$  combustor simulator for an engine component test facility is presented. The Engine Component Aero-Thermal (ECAT) facility is a full-scale engine-parts facility, designed for the study of the aero-thermal performance of fully cooled high-pressure nozzle guide vanes (NGVs). The facility operates with non-dimensionally matched engine conditions in terms of Reynolds number, Mach number, and coolant-to-mainstream pressure ratio. The combustor simulator is designed to replicate lean-burn conditions of swirl and temperature distortion upstream of the nozzle guide vanes. The purpose is to allow the study of flow capacity, aerodynamic performance (with film cooling), and thermal performance (overall effectiveness) in the presence of engine-realistic inlet distortions. The ECAT combustor simulator design builds on the work of Hall and Povey, who developed a full-scale low-speed atmospheric-pressure combustor simulator for the preliminary design of similar simulators later implemented in the Oxford Turbine Research Facility and ECAT. This pilot facility produced non-dimensional lean-burn combustor-exit conditions closely matched to target profiles representative of modern aero engines. This design was modified and scaled for compatibility with the annulus-line and higher-pressure operating conditions of the ECAT facility. In the present study, detailed experimental measurements with multi-hole probes and thermocouples (pressure profile and temperature field) are presented and compared to results from Reynolds-Averaged Navier–Stokes Simulations. Additional simulations were performed to understand how the elevated back-pressure and vane potential field affect the non-dimensional profiles of pressure loss, residual swirl, and temperature at the combustor–turbine interface. This is perhaps the most comprehensive study to date of a combustor simulator in an engine-scale research facility, providing a unique insight into the known challenges of simulator design, scaling issues when moving from low to high Reynolds number, and limitations of computational fluid dynamics in this flow environment. The results, which will serve as boundary conditions to understand the impact of this flow on components in future studies in this facility, demonstrate the fidelity with which lean-burn target conditions can be replicated in a non-reacting environment. [DOI: 10.1115/1.4056387]*

**Keywords:** lean-burn combustor simulator, facility design and validation, nozzle guide vane performance, engine-scale testing, computational fluid dynamics (CFD)

## Introduction

Lean-burn combustion has been shown to reduce emissions of carbon monoxide, nitrogen oxides ( $\text{NO}_x$ ) and particulates by avoiding stoichiometric conditions, thus lowering peak temperatures. It is therefore regarded as advantageous over traditional rich-burn architectures.

In most modern turbofan combustors, flame stabilization is achieved by swirling the flow, resulting in a region of recirculating flow (reversed axial flow). In lean-burn combustors, a far greater mass fraction of the engine core flow is involved in this swirling motion, when compared to traditional combustor architectures, resulting in a significant residual swirl, greater turbulence intensity, and a bucket-shaped temperature profile (constant across most of the span; cold near walls) at the inlet to the high-pressure (HP) turbine.

Given these altered boundary conditions, the robustness of the aerodynamic and thermal design of the high-pressure nozzle guide vane to inlet swirl, thermal profiling and unsteadiness must be carefully considered. In particular, the likely impact on the vane loading distribution, the secondary flow structure, and the vane cooling systems, both due to the internal flow redistribution on account of the altered loading, and the external flow pattern as films develop on the surface, need to be quantified. The migration of temperature non-uniformities through the vane passage may also impact the thermal loading of downstream components because of the well-known temperature segregation effect in the rotor [1].

HP stage efficiency penalties due to combined swirl and temperature distortion [2] (sometimes referred to as *hot spots* or *hot streaks*) have already been demonstrated computationally. Experimental studies have primarily focused on half-stage (NGV only), non-reacting, low Reynolds number cases with simplified geometries, because more sophisticated experiments, particularly those involving real combustors, are extremely difficult to instrument, often resulting in sparse data [3]. On the other hand, transient simulations of combustor–turbine interactions, whilst not restricted in terms of the operating point, are notoriously resource-intensive when modeling reaction kinetics at engine Reynolds numbers.

<sup>1</sup>Corresponding author.

Contributed by the Heat Transfer Division of ASME for publication in the JOURNAL OF TURBOMACHINERY. Manuscript received February 22, 2022; final manuscript received October 10, 2022; published online January 30, 2023. Assoc. Editor: James L. Rutledge.

Non-reacting combustor simulators (CS) bridge the gap between high-temperature experiments and costly simulations, allowing for the collection of comprehensive high-quality data relevant to modern lean-burn engine design [4]. In this paper, the design and experimental characterization of such a lean-burn combustor simulator for the Engine Component Aerothermal (ECAT) facility [5] is presented. The simulator is being used to study the combined impact of inlet swirl and temperature distortion on the aerodynamics (wake traverse and capacity) and thermal performance (overall effectiveness) of fully cooled nozzle guide vanes (NGVs).

## Review of Combustor Simulators With Combined Swirl and Temperature Distortion

Much of the early work on turbine inlet distortion effects focused on temperature distortion (or, so-called, *hot-streak*) effects. This work has been comprehensively reviewed in the literature [4]. Other studies contributed to understanding of the effect of turbulence [6,7], because of increasing awareness of the significant non-uniformity of turbulence at the outlet of rich-burn combustors.

Swirl-stabilized lean-burn combustors are a relatively recent innovation, and the literature is therefore limited. The first studies to develop swirl simulators for turbine experiments were focused on understanding the impact of swirl—in isolation—on turbine performance and heat transfer [8–10]. Understanding of the impact on secondary flows led to a realization that swirl and temperature distortion could *not* be dealt with by superposition [2], and this mandated the use of combined simulators in experiments. This second wave of experiments was aimed at understanding the combined impact (swirl and temperature profile) on turbine performance and on the aerodynamic and heat transfer performance of NGVs and the HP turbine. As part of the analysis, the swirl-induced migration of the temperature pattern through the vane and rotor has been studied numerically [2,11], and the results proved to be interesting, if disappointingly geometry-specific. The literature on combined simulators is briefly reviewed.

Investigators at the University of Florence (UNIFI) completed several studies on a tri-sector (3/20 annular sector) CS, which implemented the Full Aerothermal Combustor-Turbine InteractiOns (FACTOR) combustor geometry. The facility acted as a precursor to the fully annular Next Generation Turbine Test Facility [12,13], which integrates the same CS in a state-of-the-art 2.5 stage rotating test-rig. In both facilities, temperature distortion is introduced through multiperforated effusion-cooled liners, closely mimicking how coolant is introduced in a real engine. The compact design of the tri-sector facility, first presented by Koupper et al. [14], was successfully validated with large Eddy simulations (LES), demonstrating sufficient similarity in outlet profiles obtained when using a tri-sector design as opposed to a full ring of swirlers. Surveys at combustor exit, using both thermocouples, multi-hole probes [15], and hot-wire anemometry [16], to study the unsteady flow field, showed promising similarities between the target and experimental swirl profiles. However, initial results highlighted the necessity for a cylindrical tube mounted at the exit of the swirler to prevent premature mixing of the heated mainstream flow with coolant streams to guarantee a lean-burn-representative non-dimensional temperature profile [15].

A similar topology was implemented in the Demonstrator Lean-burn Combustor Simulator (DLCS) [17], on which the present work is based. Whilst temperature distortion was introduced through annular cold air bleed slots at hub and case (instead of the effusion-cooled liner employed in the UNIFI tests), a diffusion tube, fitted at the exit of the flat blade swirlers, controlled the axial deceleration rate to reduce the likelihood of vortex breakdown as the flow mixes out to fill the annulus. Another innovative feature of the DLCS was the axial orifice at the center of each swirler, which was successfully used to generate a jet that suppresses the formation of a precessing vortex core (PVC) without disturbing the desired inlet total pressure field. A PVC is an undesirable large-scale, asymmetric, corkscrew-shaped coherent flow feature, which is often

associated with catastrophic hydrodynamic instability of the combustion process [18]. It is thus perhaps surprising that PVC suppression was not considered part of the UNIFI experiment. In real engines, such features are thought to be largely suppressed by a combination of combustion-induced volume dilation through heat-release and conscious design choices [19], thus necessitating an artificial means of eliminating them in non-reacting facilities such as the DLCS. The simulator was characterized experimentally [20], by conducting detailed traverse measurements at atmospheric exit pressure over three swirler pitches. Well-defined swirl and temperature profiles were achieved, which were a good match for the target profiles and pre-test unsteady-Reynolds-averaged Navier–Stokes simulations. In a similar upgrade program to that described in the current paper, a DLCS was implemented and commissioned [21] in the Oxford Turbine Research Facility (OTRF). The facility was subsequently used to characterize the effect of lean-burn combustor flows on a 1.5-stage high-pressure turbine [22].

Parallel work on the UNIFI CS included several LES investigations performed for the purpose of comparing turbulent timescales with the experimental hot-wire data [23] and for investigating the effect of swirler-vane clocking on the development of the swirl profile [24]. The latter investigation also addressed the impact of potential field effects and the presence of NGVs on the flow at the combustor–turbine interface. These effects are important in the context of experimental measurements at the combustor outlet because they are often carried out in the absence of NGVs for improved access. The LES studies were followed by an experimental evaluation of the effect of swirl and temperature distortion on NGV film cooling [25] and aerodynamic performance [26]. More recently, the tri-sector facility was used to examine the transport and dissipation of turbulence through the NGV under lean-burn-representative inlet swirl and temperature distortion [27], reporting substantial residual swirl and turbulence downstream of the NGVs (in the HP-rotor frame of reference).

## The ECAT Facility

The ECAT facility [5] is an engine-parts facility to study high-pressure nozzle guide vanes. The parts are typically (depending on the test program) from a modern high-bypass-ratio civil turbofan engine and are operated at non-dimensionally engine representative conditions of Mach number ( $M$ ), Reynolds number ( $Re$ ), and coolant-to-mainstream pressure ratio. The facility has semi-transient operation (typically 40–60 s), operating in regulated-blowdown mode from compressed air tanks.

The mainstream flow is heated by electric heaters (2 MW), which in the current installation offer a hot-to-cold temperature ratio of approximately 1.2 (to be extended to 2.0 in an upgrade program [28]). There are auxiliary feeds to control coolant flow and dilution flow for the combustor simulator. Typical facility operating conditions are summarized in Table 1.

## Design of the Combustor Simulator

The ECAT CS is based on the pilot studies of Hall and Povey [20] in the DLCS. This design was modified and scaled for

**Table 1 Operating conditions of the ECAT facility**

Parameter	Nominal value
Vane inlet total pressure, $p_{0m}$ , bar	1.0–3.0
Vane pressure ratio, $p_{exit}/p_{0m}$	0.35–0.7
Vane exit $M$	0.7–1.3
Vane exit $Re$	$3 \times 10^5$ – $9 \times 10^5$
Coolant-to-mainstream pressure ratio	0.99–1.07
Mainstream mass flow, kg/s	6–17
Inlet total temperature, K	290–370

compatibility with the annulus-line and higher-pressure operating conditions of the ECAT facility. This required definition of the number of swirlers, blade geometry, and coolant slot areas at hub and case, based on target profiles.

The geometry of the ECAT combustor simulator is shown from a meridional view in Fig. 1(a). A compact swirler assembly and diffuser (to suppress vortex breakdown by controlling the rate of axial diffusion [17]) is mounted in a contracting annulus line that represents the relevant engine geometry. As shown in Fig. 1(b), the swirlers feature a central jet orifice to suppress the formation of a PVC [17]. The temperature profile is generated by controlled injection of coolant through annular hub and case slots. The coolant mass flow rates and coolant slot areas were optimized to achieve the target profiles of total temperature and pressure at the reporting plane, which is located 0.5 axial chords upstream of the vane leading edge at midspan (see Fig. 1(a)).

The target profiles of total pressure, non-dimensional total temperature (or *effectiveness*), swirl angle, and pitch angle were loosely defined based on those by Shahpar and Caloni [29]. Their profiles were obtained from a simulation of a lean-burn combustor prototype under reacting conditions and are hence a suitable approximation of the non-dimensional fields anticipated at the combustor–turbine interface.

**Combustor Simulator Design Optimization.** The optimization of the system is covered in Refs. [17,30]. So far as the temperature profile is concerned considerations included:

- (1) enthalpy balances in the upper and lower halves of the annulus to match the required temperature deficits for the non-dimensional profile (discussed in Ref. [30]);
- (2) the axial position of the outlet of the coolant slots with respect to the reporting plane, which controls the amount of mixing and the non-dimensional shape of the profile at the reporting plane;

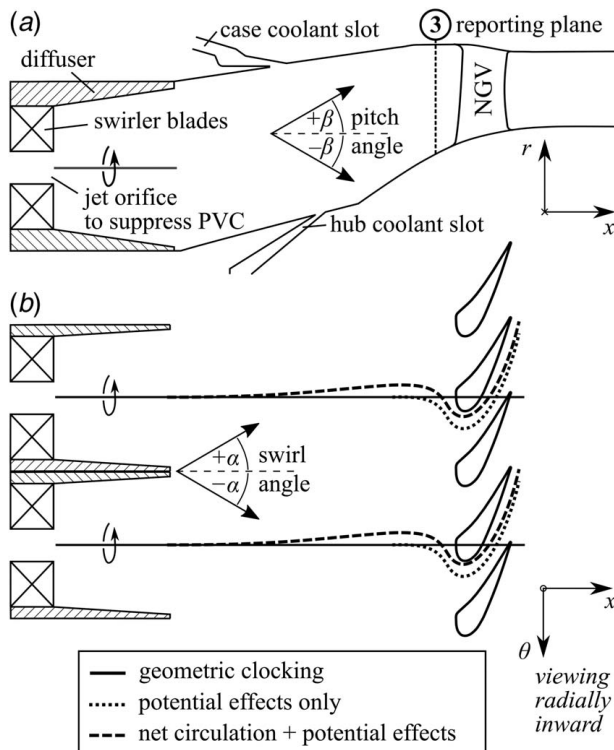


**Fig. 1 Geometry of the combustor simulator showing: (a) hub and case coolant injection slots and pitch angle convention and (b) migration of the bulk flow, clocking relative to vanes, and swirl angle convention**

- (3) the temperature ratio of the hot and cold gas at the point of injection;
- (4) the outlet areas of the hub and case coolant injection slots which controls the velocity difference between streams (controls initial shear) and the dynamic head, which controls the total pressure profile at the point of mixing, assuming continuity of static pressure at the interface between streams.

These parameters must be optimized simultaneously, and their interaction is interesting and subtle. An example of the complexity of the optimization is that a given enthalpy deficit can be achieved with a given mass flow rate of very cold gas or a larger mass flow rate of a relatively warmer gas, with the simultaneous optimization of the injection point allowing a variety of shape factors and max-to-min temperature differences in the resulting profile. Such considerations are well-covered in Ref. [30].

So far as the swirl profile is concerned, the following must be considered:

- (5) the peak angle of the individual vanes of the swirlers;
- (6) the swirler total pressure loss at the reporting plane;
- (7) the rate of axial deceleration in the diffuser tube, which can reduce the likelihood of vortex breakdown, and complete mixing out of the profile;
- (8) the contraction ratio between swirler exit and the reporting plane, which controls the swirl angle at the reporting plane through the axial velocity;
- (9) the rate of axial acceleration in the downstream annulus, which has an impact on the peak swirl angles at the reporting plane (*stretching* effect on vortex [31]);
- (10) the axial distance between the swirler and the reporting plane.

In the ECAT facility, the maximum hot-stream temperature is limited by heater power. The cold-stream air is drawn directly from a high-pressure tank at ambient temperature. Mass fractions (enthalpy balance considerations) and associated stream temperatures (practical considerations) and axial injection locations were chosen (based on computational fluid dynamics (CFD) simulations and prior experiments) to define the desired profile. At the point of injection, it is possible to design for matched velocity or matched total pressure. The first is a minimum shear condition (chosen in our case to delay mixing, but resulting in slightly elevated total pressure in the coolant layer) and the second is a design requirement for studies requiring flat inlet total pressure.

**Swirler Count and Geometry.** The CS contains 20 flat vane swirlers (versus 40 NGVs), which were designed according to the initial work of Kilik [32]. As implemented in the DLCS [17], a cylindrical orifice at the center of the swirler was used to suppress the formation of the PVC. The vane angles were estimated using a free vortex assumption between the swirler and reporting plane. Each swirler is comprised of 10 vanes, angled at 20 deg relative to the axial direction, yielding a swirl number of 0.26. The swirl number,  $S$ , was defined by

$$S = \frac{\int_0^{r_{sw}} V_x V_\theta r^2 dr}{r_{sw} \int_0^{r_{sw}} V_x^2 r dr} \quad (1)$$

where the radius,  $r$ , the axial velocity,  $V_x$ , and the tangential velocity,  $V_\theta$ , are defined in a swirler-centered coordinate frame. This parameter is commonly used to characterize the intensity of a vortex [33] and the value it takes can be considered a good predictor of whether a recirculating region might develop [34]. For  $S < 0.60$  and hence for the ECAT CS ( $S \approx 0.26$ ), the axial pressure gradient is too weak to cause flow recirculation [34]. Whilst in most modern combustors  $S$  is greater than 0.60 (to anchor the flame), the absence of volume dilation-induced acceleration in the ECAT CS mandated a lower swirl number to achieve the target swirl angles at the reporting plane, given the fixed contraction ratio of the annulus line and physical dimension of the NGVs. The swirlers were clocked as in



the engine, such that the central axis of each swirler was geometrically aligned with the midspan stagnation point of alternating NGVs. This is illustrated in Fig. 1(b). The integer-multiple periodicity simplifies the CFD setup.

## Combustor Simulator Commissioning

**Geometry and Hardware.** An engine-scale, high-pressure CS was designed and manufactured for the ECAT facility. A photograph of the hardware is shown in Fig. 2. Five struts support the test section core, which houses the hub feed lines for the combustor simulator and the vane ring.

**Instrumentation.** A schematic of the general arrangement of the test section is shown in Fig. 3. Heated mainstream air from the axial stiffener passes through the swirlers and the diffusers. Further downstream, cold air is introduced from annular slots at hub and casing before the contraction shapes the swirl profile. Also indicated in Fig. 3 are the locations of the three key measurement planes. A detail of measurement planes 2 and 3 is presented in Fig. 4. The instrumentation at each of the three planes is now briefly outlined.

At planes 1 and 2, two pairs of Pitot probe and bare bead thermocouple rakes are used for routine monitoring. At plane 1, probes in two circumferential locations measured a total of six pressures and six temperatures, which serve as reference conditions for the temperature and pressure normalization. At plane 2, probes with eight radially staggered measurement points were located at four circumferential positions (each for pressure and temperature) giving a total of 32 pressure and 32 temperature measurements within the combustion chamber. The hub and case coolant plena pressures and temperatures were measured using two pressure and temperature points located diametrically opposite to one another (two of each type per plenum).

At plane 3 (reporting plane), aerodynamic traverse measurements were taken with a five-hole probe, a ducted three-hole probe

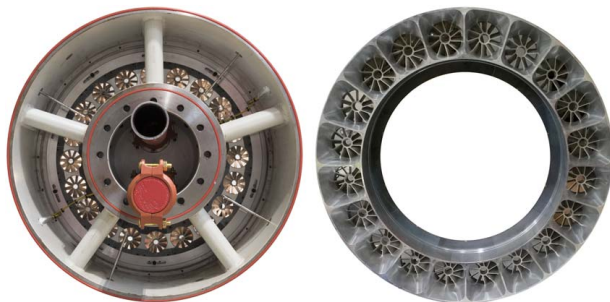


**Fig. 2** Photograph of the combustor simulator viewed from upstream (left) and downstream (right). The upstream struts, swirlers, and diffusers are visible.

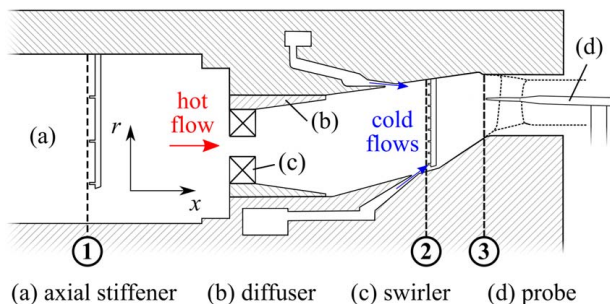


**Fig. 3** Schematic of the general arrangement of the combustor simulator, showing the hot and cold feeds. The position of the measurement planes 1, 2, and reporting plane 3 are shown, as is the outline of the (removed) vane ring.

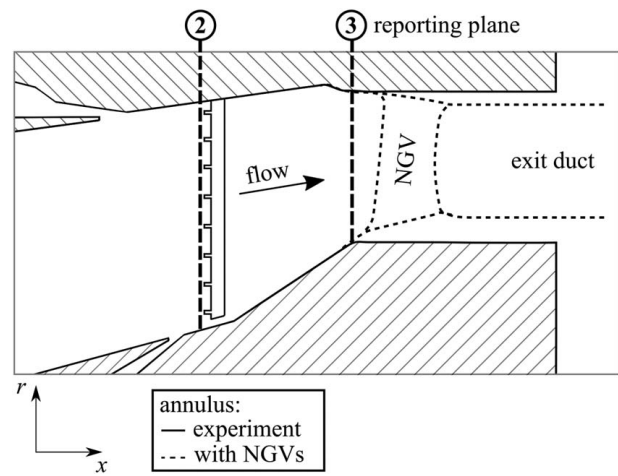


**Fig. 4** Detail of measurement planes 2 and 3, showing the NGV position (removed in these experiments)

(sensitive to swirl but not pitch), and a bare-wire thermocouple probe (25  $\mu\text{m}$  bead diameter). The five-hole probe was used to survey the central 80% span, whilst a three-hole probe was used for the top and bottom 10% of span, allowing measurements of yaw angle very close to the walls (the three-hole probe does not report pitch angle). The hub-mounted traverse equipment has been described in Refs. [5,35,36]. The traverse was configured to cover an annular sector of 40 deg in a single run but can be clocked at 36-deg increments allowing the entire annulus to be traversed. To determine acceptable traverse speed, the pressure probe-system time constant was determined using the methods discussed in Ref. [37], whilst the thermocouple probe was designed according to Ref. [38]. The effective bandwidth of the pressure and temperature signals was estimated to be around 50 Hz. Pneumatic tubing lengths were minimized by mounting the transducers on the traverse. A digital zero-phase filter was applied to the signals, both sampled at 500 Hz. The probes were traversed circumferentially (constant spanwise position) at 4 deg per second, giving a passing time of 4.5 s for a single swirler pitch. This is equivalent to a spatial resolution of 0.5 mm in the circumferential direction, or 225 samples per swirler pitch. The effect of the traverse motion on the measurements was verified to be negligible by performing several sweeps in alternate directions and overlaying the left- and right-passing events to ensure zero positional offset between them. The radial resolution (step height) was set to 4.5% of passage height over most of the span (3.1 mm) reducing to 2.3% (1.6 mm) for the upper and lower 10% span.

## Experimental Conditions for Commissioning Experiments.

To allow detailed traverse measurements at the reporting plane, experiments were conducted without NGVs installed, and with a modified exit duct to improve probe access (illustrated in Fig. 4). If the NGVs had been installed, the extremely low dynamic-to-total pressure ratio in the combustor simulator would result in an unacceptable signal-to-noise ratio for five-hole probe measurements. Without NGVs, the back-pressure during testing was approximately atmospheric (compared to an absolute pressure of 1.80 bar at nominal conditions, with NGVs installed). Further experimental conditions are summarized in Table 2.

Typical inlet pressure ( $p_{01}$ ) and temperature ( $T_{01}$ ), measurements at plane 1 and in the coolant plena ( $p_{0c}$  and  $T_{0c}$ ) are shown in Fig. 5. The coolant and mainstream mass flow rates are slowly increased by opening a valve (24–30 s). To prevent accidental damage, the heaters are only switched on once the mass flow is sufficiently high, leading to a sudden increase in  $T_{01}$  (34 s). Although maximum power is reached in less than 2 s, the mainstream temperature characteristic during the heated part of the run is asymptotic,

**Table 2 Operating conditions for experiments**

Parameter	Value
Mainstream (hot) mass flow, $\dot{m}_h$ , kg/s	11.60
Coolant mass flow, $\dot{m}_c$ , kg/s	1.54
Case coolant mass fraction	0.58
Hub coolant mass fraction	0.42
Inlet total temperature, $T_{0h}$ , K	330–350
Coolant total temperature, $T_{0c}$ , K	290–295
Exit plane absolute static pressure, bar	1.0

on account of the thermal mass of the pipework and settling tanks between the heaters and plane 1 (this is modeled in Ref. [28]). Once the heaters are at full power and  $p_{01}$  is stable, the traverse is started manually at 41 s. The flow at plane 1 (at the outlet of the settling tank) and in the coolant plenum is well-mixed and can be assumed to be spatially uniform, though varying in time. Throughout the run, the coolant temperature decreases slightly owing to the expansion of gas in the high-pressure tank. At 84 s, the heaters are switched off automatically, followed shortly by the closure of the main valve at 87 s.

The temperature measured at the reporting plane,  $T_{03}$ , is presented as effectiveness,  $\eta^*$ , defined by

$$\eta^* = \frac{T_{03} - T_{0c}}{T_{01} - T_{0c}} \quad (2)$$

where the hot reference temperature,  $T_{01}$ , is measured at plane 1 (upstream of the swirler) and the cold reference temperature,  $T_{0c}$ , is that measured in the coolant plenum. This definition is convenient for combustor simulators because the hot and cold temperatures are easy to measure.

In principle, therefore, the non-dimensional temperature could be calculated—in real time—at the reporting plane. The issue arises, however, that there are additional thermal masses (the metal walls), with associated heat transfer from the hot gas to the cool walls, between plane 1 measurements and the reporting plane measurements. To understand the data at fixed thermocouple locations at plane 2, and to correctly normalize the traverse data at plane 3, it is necessary to account for the inter-plane heat losses. This is particularly true for traverse data at plane 3, because, in addition to the transients due to the thermal mass between planes 1 and 3, the probe is moving through a spatial field of temperature (from

coolant injection). Thus, decoupling the two effects is impossible without a *transient heat transfer correction*. This correction is discussed in the following section.

**Transient Effectiveness Correction.** The experimental effectiveness,  $\eta^*$ , is corrected based on the expectation that the midspan region at plane 3—being devoid of coolant—will experience an effectiveness of unity under adiabatic conditions (as observed in complementary CFD simulations), such that any deficit may be attributed to transient convective heat loss. A scalar, time-dependent correction factor,  $k_{\text{corr}}$ , is defined based on a curve fit to an ensemble average of the uncorrected reporting plane effectiveness in the 30–70% span region across all runs. Thermal traverse data are aligned in time using a run-specific temporal offset,  $\delta_i$ , to ensure that the instant at which the heater switches on coincides between runs. The correction factor is obtained by fitting an analytically based one-dimensional (1D) solution to the ensemble average of the time-aligned traverse data

$$k_{\text{corr}}(t - \delta_i) = 1 - ae^{[b(t-\tau)]} \text{erfc}\left(\sqrt{|b(t-\tau)|}\right) \quad (3)$$

The generic form corresponds to the non-dimensional fluid outlet temperature under a step change in inlet temperature at time  $\tau$ , assuming a constant heat transfer coefficient for convective heat loss to a one-dimensional, semi-infinite wall [39]. Symbols  $a$ ,  $b$ , and  $\tau$  represent the least-squares optimization parameters. The averaged traverse data and correction factor curve are shown in Fig. 6.

In Fig. 6, the traverse average effectiveness increases throughout the run because the test section heats up, thus reducing the driving temperature difference, which causes heat loss between plane 1 and plane 3. Despite averaging the traverse data across multiple runs, minor oscillations persist due to a strong correlation between the circumferential position of the probe,  $\theta$ , and pseudo-time,  $t - \delta_i$ , resulting in simultaneous exposure to the same circumferential thermal non-uniformities (albeit at different radii). The high-frequency oscillation is caused by the thermal wakes of diffuser walls between adjacent swirlers whereas the lower frequency but higher amplitude oscillation arises from the thermal wake of a large upstream strut (see Fig. 2). Both features are absent in adiabatic CFD simulations but were successfully reproduced in constant (cold) wall temperature simulations (not presented), confirming they are purely a consequence of transient heat transfer. The wake of the upstream strut is discussed further in the results section.

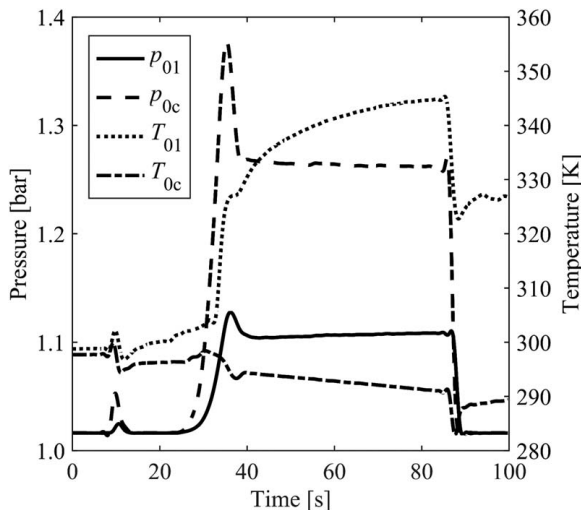


**Fig. 5 Typical inlet pressure and temperature measurements at plane 1 and in the coolant plenum**

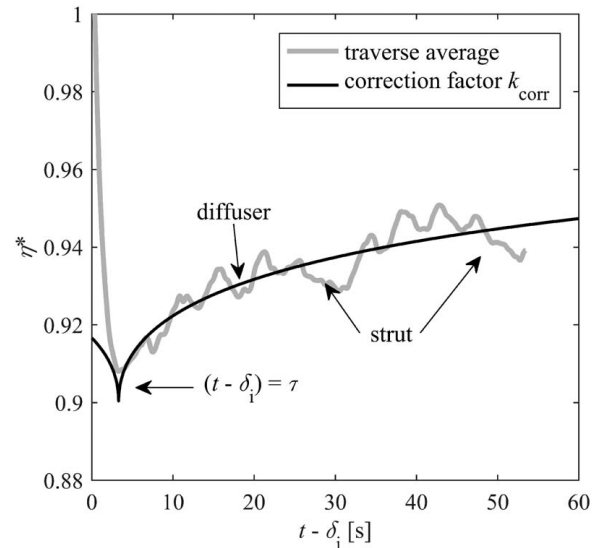


**Fig. 6 Correction factor fit to average of reporting plane thermocouple traverse runs in the 30–70% span range**

We define the corrected equivalent mainstream effectiveness,  $\eta_{\text{corr}}^*$ , by

$$\eta_{\text{corr}}^*(t) = \frac{\eta^*(t - \delta_i)}{k_{\text{corr}}(t - \delta_i)} \quad (4)$$

The instantaneous effectiveness from each individual run—including those outside of the 30–70% span range—is scaled by dividing by factor  $k_{\text{corr}}$  (with run-specific temporal offset  $\delta_i$ ). Radial profiles of corrected and uncorrected effectiveness at the reporting plane are compared to results from an adiabatic CFD simulation in Fig. 7.

It is evident that the correction method effectively eliminates the overall enthalpy deficit as well as saw-tooth discontinuities in radial profiles at the interface between adjacent area traverses. The similarity between adiabatic CFD and experimental results in the near-wall region is also improved. Minor oscillations persist in the corrected data because the transient heat loss is a function of both space and time. Spatial variations in heat loss cannot be captured by the scalar, time-dependent correction factor, because insufficient data is available to construct a higher order correction model.

## Numerical Methods

In this section, the CFD analysis performed to investigate the effect of increased back-pressure as well as that of the vane potential field on the swirl profile and circumferential flow migration is described.

**Computational Fluid Dynamics Domains.** For the detailed CFD analysis, two computational domains were generated: one excluding and another including vanes. Together, they enable assessment of the validity of using the present experimental results at vane inlet as a reference condition in future studies *with vanes*.

The domain extends to the inlet of the axial stiffener (see Fig. 8) because swirler lip separations, which would otherwise not be captured, were observed to have important effects on the development of loss within and downstream of the swirler passage. This approach was seen to offer an improved prediction of total pressure loss over a circular duct-fed swirler approach. Circumferentially, the computational domains span two vane passages or one swirler pitch.

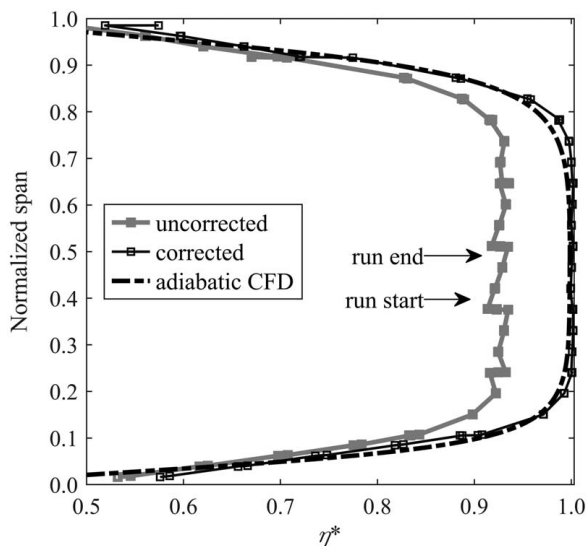


**Fig. 7** Uncorrected experimental versus corrected experimental versus low-pressure CFD  $k$ - $\epsilon$  radial effectiveness (adiabatic simulation)

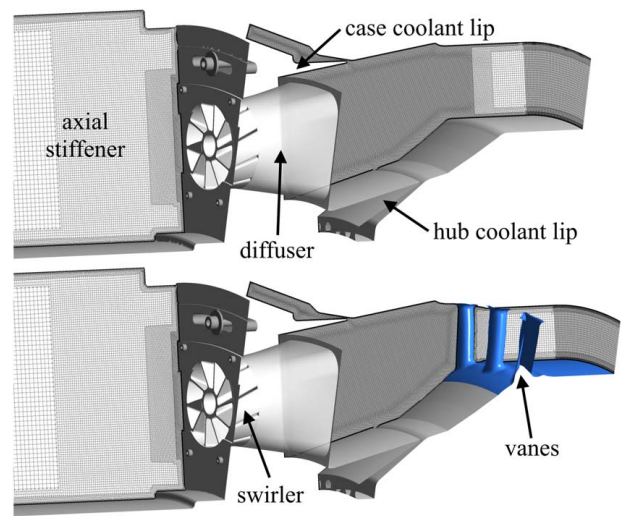


**Fig. 8** Meshed flow domains with and without NGVs

The geometric differences between the two domains (presence of the vanes and altered exit duct geometry) are shown in Fig. 8.

**Numerical Test Matrix.** The three CFD cases that were run are summarized in Table 3. They are now briefly described.

The first case replicates the experimental conditions, enabling direct comparison of profiles at the reporting plane whilst also establishing a baseline for the accuracy of various turbulence models. The measured profiles were obtained without NGVs installed and with atmospheric pressure at the rig exit. The second case also excludes the NGVs but was performed at elevated exit pressure to emulate the increased back-pressure that would arise in the presence of downstream vanes. The third case is both at elevated pressure and includes vanes. In combination with the second case, it serves to isolate vane potential field and back-pressure effects.

**Mesh and Boundary Conditions.** A hybrid meshing approach, which included the generation of hexahedral elements in the free-stream region, tetrahedral element around complex features, and prisms within the boundary layer regions, was particularly suited to the complex geometry of the combustor simulator. The meshes without and with NGVs, comprised of 67 million and 87 million cells respectively, are effectively identical upstream of the vanes. Both grids were refined near the walls, featuring 24 prism layers with an expansion ratio of 1.2. The grid sensitivity was evaluated by refining both meshes globally by decreasing the background cell size of the octree mesh. This is discussed in Appendix A. Results are shown for the most refined meshes.

For all cases, the mainstream and coolant mass flows applied at the inlets are matched to the experimental conditions in Table 2,

**Table 3** Description of CFD cases

CFD Case	Domain + exit pressure	Purpose
1	without NGVs, at low exit pressure (1 atm)	for direct comparison with ECAT combustor commissioning experimental results
2	without NGVs, at high exit pressure (2.0 atm)	to decouple potential field and back-pressure effects
3	with NGVs, at low vane exit pressure (1 atm)	to predict effects of the presence of NGVs on inlet profiles



with corresponding total temperatures set to 350 K (mainstream) and 290 K (coolant feeds). Having carried out a sensitivity study and concluded no significant dependence of the flow on the inlet turbulence, the intensity was set to 5% at all inlets. A 1:1 rotational periodic interface was used at the circumferential extents of the domain. For cases 1 and 3, the exit pressure was atmospheric, whereas the back-pressure for the second case (without NGVs) was determined from the pressure which naturally develops in the plenum of case 3 (approximately 2.0 bar, depending on the turbulence model). The local pressure at the outlet was calculated from the radial equilibrium equation. All walls were modeled as smooth and adiabatic.

**Models and Solver Settings.** All CFD simulations were performed in ANSYS CFX 20.2. Simulations were run in double-precision with a steady, compressible solver. Simulations for three turbulence models— $k-\varepsilon$  [40],  $k-\omega$  SST [41], and the SSG Reynolds Stress Model (RSM) [42]—were performed. Scalable wall functions were used for  $k-\varepsilon$  and SSG RSM, whereas the  $k-\omega$  SST model utilizes enhanced wall functions to adaptively switch between a wall-resolved and wall function approach, depending on the local value of  $y^+$ . This approach allowed the use of the same grid for all three models. For  $k-\varepsilon$  and  $k-\omega$  SST, a second-order blended discretization was employed for both the momentum equations and turbulence. The SSG RSM model was only stable using first-order turbulence numerics.

## Experimental and Numerical Results

In this section, we compare experimental and numerical results at the experimental condition (atmospheric exit pressure without NGVs installed).

The measured total pressure maps are presented in terms of a swirler total pressure loss coefficient,  $C_{p,sw}$ , defined by

$$C_{p,sw} = \frac{p_{01} - p_{03}(r, \theta)}{q_{sw}} \quad (5)$$

$$q_{sw} = \frac{\dot{m}_h^2}{2A_{sw}^2 \rho_1} \quad (6)$$

Here,  $p_{01}$  and  $p_{03}$  are the total pressures at planes 1 and 3, respectively. The denominator,  $q_{sw}$ , is the reference dynamic pressure, which is defined in Eq. (6), using the hot mass flow,  $\dot{m}_h$ , the swirler reference area,  $A_{sw}$ , and the density at plane 1,  $\rho_1$ . The expression follows from the one-dimensional continuity equation, assuming incompressible flow. Experimentally, the pressure difference  $p_{01} - p_{03}(r, \theta)$  was measured with a differential transducer setup to reduce the bias uncertainty of the total pressure loss coefficient (estimated to be  $\pm 3.8\%$  to  $2\sigma$ ).

The temperature normalization has previously been described in Eq. (2). All effectiveness data in this section has been corrected according to the definition of  $\eta_{corr}^*$  in Eq. (4). The  $2\sigma$  (95%) confidence interval for the experimental effectiveness was estimated at  $\pm 3.5\%$ , assuming temperature measurements have a standard error of  $\pm 0.73$  K.

The swirl angle,  $\alpha$ , and the pitch angle,  $\beta$ , are defined as follows:

$$\alpha = \arctan\left(\frac{V_\theta}{V_x}\right) \quad (7)$$

$$\beta = \arcsin\left(\frac{V_r}{V}\right) \quad (8)$$

where  $V$  is the local velocity magnitude and  $V_r$ ,  $V_x$ , and  $V_\theta$  the radial, axial and circumferential components, respectively, in the machine

reference frame. The sign convention for flow angles is indicated in Fig. 1(b). The  $2\sigma$  confidence interval for flow angles was estimated to be  $\pm 1.6$  deg, based on the alignment uncertainty during probe calibration and testing (both were assumed to be uniformly distributed between  $\pm 1$  deg).

Figure 9 is a side-by-side comparison of the experimental results and the  $k-\varepsilon$  CFD simulation for the low back-pressure case (without NGVs), showing profiles of total pressure loss coefficient, equivalent mainstream effectiveness, swirl angle, and pitch angle.

**Distributions of Loss, Temperature, Pitch, and Yaw.** Consider first the total pressure loss coefficient distributions. In both the experiment and CFD, oval-shaped regions of relatively high loss are observed near the midspan, peaking approximately one-fifth of a swirler pitch (or 3.6 deg) to the left of the swirler geometric centerlines. Both experiment and CFD have elevated total pressure (reduced  $C_{p,sw}$ ) close to the end walls due to the slot injection of coolant.

At the casing, immediately to the right of the swirler centerlines, this region protrudes slightly into the mainstream. A corresponding, but less distinct feature can be seen at the hub. The most natural explanation for this effect would be upwash of the (relatively) high-pressure coolant at the vortex–vortex interface. CFD streamlines indicate, however, that the feature originates from the root region of the swirler blades. The streamlines passing through this region experience lower than average total pressure loss because the flow at the root region of the swirler remains attached, whereas large-scale flow separation occurs along the outer span of the swirler vane suction side well as the shroud. Overall, there is an excellent match between the experimental and CFD data.

Consider now the corrected equivalent mainstream effectiveness ( $\eta_{corr}^*$ ) data. The dominant feature in both experimental and CFD data is the relatively cold (low  $\eta_{corr}^*$ ) flow near the hub and case walls, indicating well-behaved near-wall coolant flow. The coolant layer at the case is slightly thicker than that at the hub due to a higher injected coolant mass fraction. There is a periodic thickening in the coolant layer at both the hub and case, with the same periodicity as the swirler count and the thick regions largely coinciding with regions of elevated total pressure. This is in line with the argument that the high-density coolant is the primary influence on the total pressure field in the near-wall regions. Overall, the CFD matches the experimental effectiveness profile extremely well, producing a nearly identical radial profile (see Fig. 7). The only significant dissimilarity is the region marked as “thermal wake” at approximately  $\theta/\theta_{sw} = 4$ . This is caused by convective heat loss to an upstream radial strut (see Fig. 2, and discussion regarding the transient correction to equivalent mainstream temperature). The strut is aligned with the swirler geometric center  $\theta/\theta_{sw} = 4$ , and the cold thermal wake appears to be “processed” by the swirler into a diagonal strip approximately downstream of that swirler. This feature is not captured in the CFD, because the domain covers a single swirler sector, and the radial strut is not modeled.

We now consider the swirl angle ( $\alpha$ ) distribution (sign convention in Fig. 1). The experimental swirl angle distribution is very periodic, confirming well-behaved vortex cores with minimal non-periodic interaction between them. The iso-line of zero swirl has a quasi-sinusoidal profile, characteristic of distorted (non-circular) vortex cores. The CFD results are similar in general form, with rather less distortion from a regular (circular) vortex than the experimental data.

Finally, consider the pitch angle distributions. As expected, the trend is for mildly negative pitch at the casing and positive pitch at the hub, in line with the annulus hade angles (see Fig. 4), with the classical quasi-sinusoidal variation of the iso-line of zero pitch associated with the interaction of the vortex with the annulus hade. The general pattern was reasonably well matched by CFD. The experimental data for pitch angle only extends to within 10% span of the hub and case walls (probe size restriction).

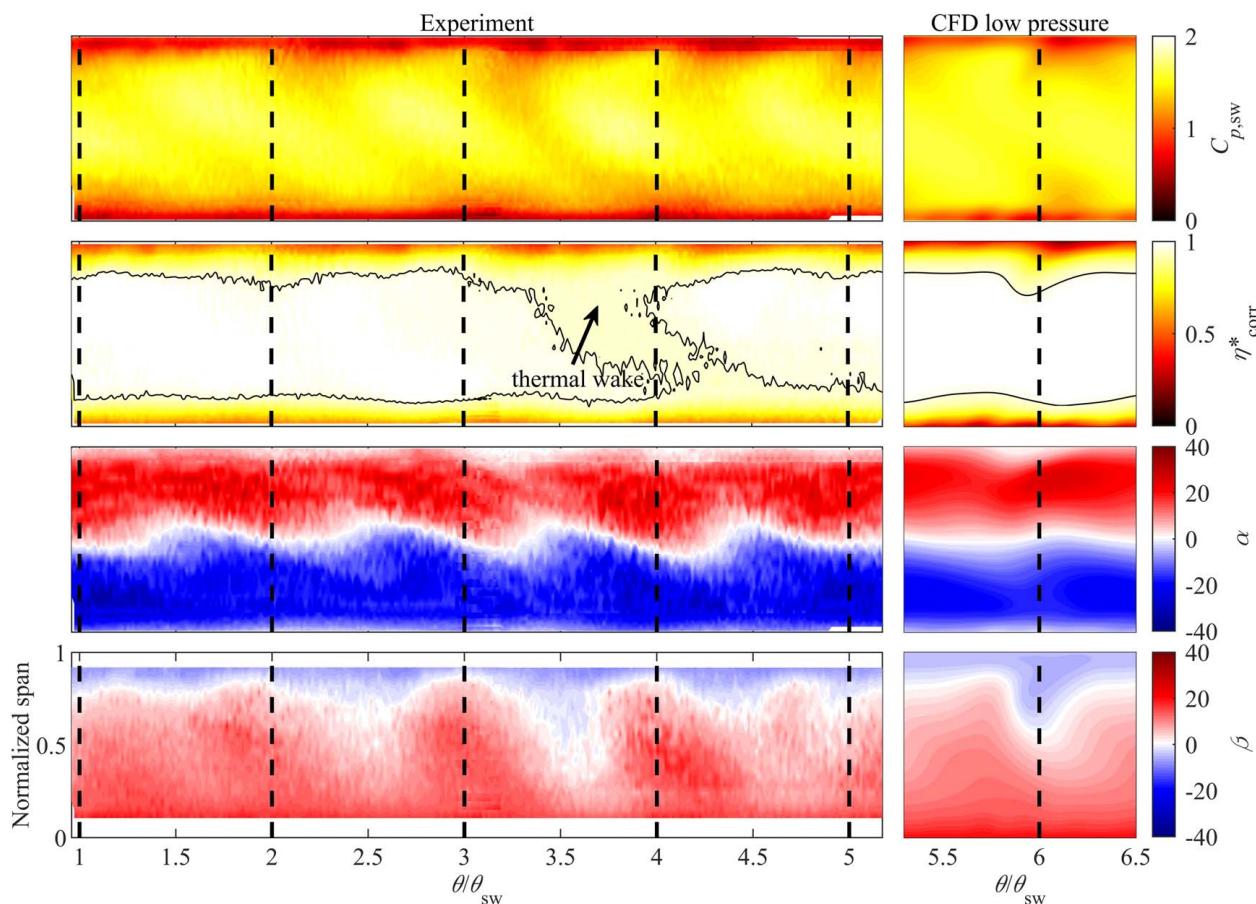


**Fig. 9** Experimental and CFD results ( $k-\varepsilon$  low-pressure case) at reporting plane 3 for loss coefficient,  $C_{p,sw}$ , corrected equivalent mainstream effectiveness,  $\eta_{corr}^*$ , swirl angle,  $\alpha$ , and pitch angle,  $\beta$ . Results are viewed from upstream to downstream. Dashed lines indicate radial lines passing through swirler centerlines.

In the next section, the radial profiles of loss coefficient, equivalent mainstream effectiveness, yaw angles, and pitch angles are considered.

**Radial Profiles of Pitch and Yaw.** Experimental and CFD-predicted radial distributions of circumferentially-averaged total pressure loss coefficient, effective mainstream effectiveness, yaw angle, and pitch angle are presented in Fig. 10. CFD data are presented for three simulations using  $k-\varepsilon$ ,  $k-\omega$  SST, and RSM SSG turbulence models using experimental boundary conditions (see case 1 description in Table 3).

First, consider the radial loss coefficient ( $C_{p,sw}$ ) profiles in Fig. 10(a). In the experimental profile, the peak loss is at approximately midspan, but with fairly uniform loss distribution between 20 and 80% span. Significantly lower loss near the walls is associated with the coolant layers, which have higher density and higher velocity than the mainstream flow (see also the distributions of Fig. 9). Predicted mass-averaged loss coefficients differ significantly between the three turbulence models, with values of 1.40 for  $k-\varepsilon$ , 1.54 for  $k-\omega$  SST, and 1.78 for RSM SSG. It is interesting to note that although both  $k-\omega$  SST and  $k-\varepsilon$  models use the  $k-\varepsilon$  equations in the freestream, the  $k-\varepsilon$  model predicts a 10% lower mass-average freestream loss, yielding a better match with experimental results.

Now consider the radial effectiveness ( $\eta_{corr}^*$ ) profiles in Fig. 10(a). The experimental profile is uniform between 20 and 80% span, where the effectiveness is unity (hot-stream temperature). Above 80% span and below 20% span, the effectiveness falls rapidly through the mixing coolant layer, to a value of approximately 0.4 at the walls. All three radial distributions from CFD simulations

are a reasonable match to the experimental distribution, with a slightly closer agreement in the hub region for the  $k-\varepsilon$  model than for  $k-\omega$  SST and RSM SSG models, both of which underpredict mixing.

Now consider the radial swirl angle ( $\alpha$ ) profiles of Fig. 10(b). The experimental profile tends to zero swirl at the walls (due to axial injection of coolant at hub and case) and at the vortex center (approximately 50% span) with maxima and minima of approximately +20 deg and -22 deg at span fractions of 0.15 and 0.83, respectively. This represents a good match to the target profile [29] (swirl angles between -20 deg and +15 deg). The  $k-\varepsilon$  CFD simulations produce a good match with the experimental data, agreeing to be within 4 deg of the measured profile across the entire span. The CFD simulations using the  $k-\omega$  SST and SSG RSM turbulence models underestimated mixing, as evidenced by a distinct vortex dipole at the reporting plane, which is not seen in the experimental data. Swirl-number-dependent accuracy of RSM has been observed by Escue and Cui [43]. At the relatively low ECAT CS swirl number (0.26), the standard  $k-\varepsilon$  model appears to offer the best overall match to experiments among the models tested.

Finally, consider the pitch angle ( $\beta$ ) profiles of Fig. 10. As expected, the trends are broadly linear (long-range potential field disturbance of the endwalls) with limits at the hub and case walls matched to the pitch angle of the annulus lines. Note that in our definitions of angle—Eq. (8)—ratios of velocity are with respect to absolute flow velocity not axial velocity, so the good match of pitch angle to the annulus pitch angle is only true in the limit of zero swirl angle at the walls (a condition that is met in the current study). The predicted pitch angle distributions were similar for all three turbulence models and were in agreement with the experimental profile to within 3 deg.



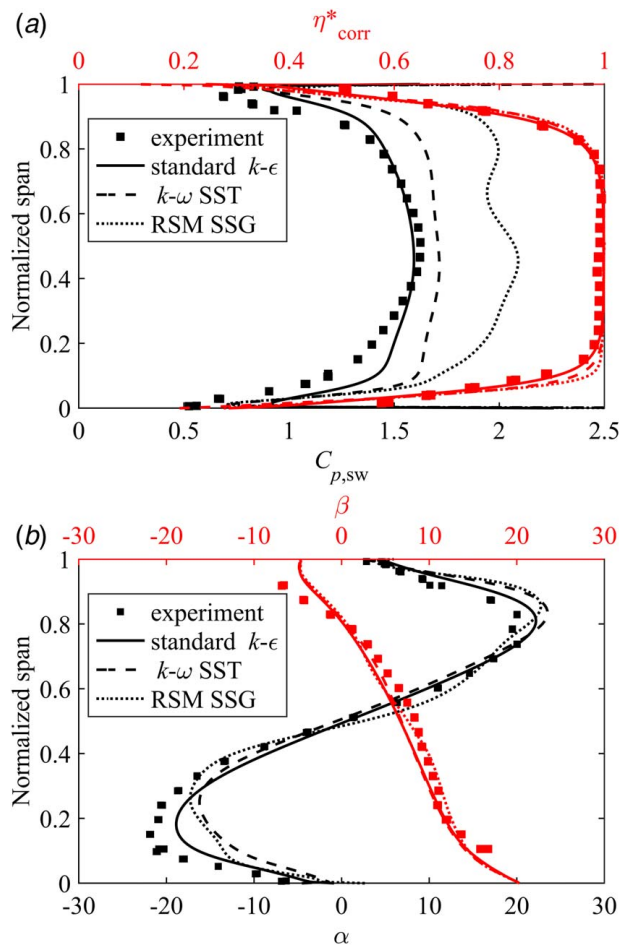


**Fig. 10 Experimentally-measured and CFD-predicted radial profiles of circumferentially-averaged: (a) pressure loss coefficient and corrected equivalent effectiveness and (b) swirl and pitch angle**

### Effect of Mach Number Mismatch and Vane Potential Field

It will be recalled the experimental data was collected with the facility operating without vanes (to allow a large sector of data to be taken at fine resolution) and with atmospheric back-pressure (improved dynamic head-to-total pressure ratio). These are clear compromises, but avoid the problems seen in previous studies [8,21] leading to sparse data, or data with high error, namely, low dynamic to total pressure ratio leading to high absolute error, transducer-line frequency response issues [37], and access. Avoiding these problems in the experimental design allowed extremely accurate data to be taken. In this section, we assess the scaling compromises associated with running the facility in this way. In particular, the sensitivity of the flow distributions to back-pressure and the NGV potential field are investigated.

**Reynolds and Mach Number Scaling.** The combustor simulator survey data were taken at the same nominal mass flow rates as a typical ECAT experiment (high back-pressure) but at lower back-pressure. We now consider how this affects swirler  $Re$  and  $M$ . Here, we define these as relevant to the flow through the swirler vanes.

The relationship between  $Re$  and mass flow rate is given by

$$Re = \frac{\rho V D_{sw}}{\mu} \propto \frac{\dot{m} D_{sw}}{\mu} \quad (9)$$

where  $\rho$  and  $\mu$  represent the fluid density and dynamic viscosity, respectively.  $D_{sw}$  is the swirler diameter (an arbitrary swirler

reference length) and  $\dot{m}$  the swirler mass flow rate. The proportionality is valid for a fixed area (relevant to all our experiments and CFD). The conclusion is that the flow pattern should be similar between the low and high-pressure cases and that the loss coefficient,  $C_{p,sw} = f(Re)$ , would be the same in both cases. Here, we reference incompressible arguments. For completeness, we note that for fixed  $\dot{m}$ , halving the absolute pressure has the effect of doubling  $\rho V^2$ . That is, the absolute loss is twice as high for the low-pressure case.

In the simplest model of free-jet loss (dynamic head mixing out), this problem could be regarded as quasi-incompressible. Certainly, the flow is well-outside the range in which shock waves would enter consideration. Interestingly, however, although the mass-flow-averaged Mach numbers at the swirler exit for the high-pressure and low-pressure  $k-\epsilon$  cases were 0.20 and 0.42 respectively (i.e., fairly incompressible for a problem of this type), the corresponding *peak* Mach numbers (evaluated from CFD) were 0.26 and 0.62. This non-uniformity arises because of two effects. Firstly, the relatively low-pressure vortex core at the center of the swirler draws in high-pressure upstream air through the axial orifice, thus increasing the Mach number of the jet. Secondly, separation-induced blockage in the swirler passages reduces the effective flow area (for a fixed mass flow), thus leading to greater flow speeds to satisfy continuity. For the low-pressure case, this represents a deviation between the *impact pressure* (difference between total and static pressure in a compressible flow) and incompressible dynamic pressure of 9.6% at the peak Mach number. A modified definition of the loss coefficient,  $C'_{p,sw}$ , is introduced to reconcile the results for the high- and low-pressure cases by accounting for local compressibility. The modified definition is given by

$$C'_{p,sw} = \frac{p_{01} - p_{03}(r, \theta)}{q'_{sw}} \quad (10)$$

where  $q'_{sw}$  is the CFD mass-flow-averaged impact pressure at the exit of the swirler. The modification decreases the loss coefficient for the low-pressure  $k-\epsilon$  case by approximately 10%, relative to the equivalent high-pressure case, when compared to the incompressible definition. In the following section, we compare the profiles at the reporting plane for the three CFD cases outlined in Table 3.

**Effects of Back-Pressure (on  $M$ ) and the Vane Potential Field.** Figure 11 serves as a direct comparison between the profiles at the reporting plane, with the three CFD cases summarized in Table 3 arranged by columns. The mass-flow-averaged Mach number at the swirler exit is indicated at the top of each column. Due to limited space, only the results for  $k-\epsilon$  are shown, considering this model was seen to achieve the best match with experiments.

The first row of Fig. 11 shows contours of the corrected swirler total pressure loss coefficient,  $C'_{p,sw}$ . Comparing the low back-pressure case (column 1) to the high-pressure ones (columns 2 and 3), no obvious difference in the loss is apparent, and the distribution of the flow features matches well. This is consistent with the earlier argument that at subsonic speeds, the loss coefficient is expected to scale only with the Reynolds number (which is identical for all three cases). The mass-flow-averaged total pressure loss coefficient is 0.485 for the low-pressure case, 0.479 for the high-pressure case without vanes, and 0.466 for the case with NGVs (also at high back-pressure). Here, it should be noted that the back-pressure for the second case was set based on the combustor pressure from the third case, which was simulated with atmospheric exhaust pressure (but with vanes), allowing the back-pressure in the combustor simulator to develop naturally. With both  $Re$  and  $M$  matched, any differences between cases two and three are thus due to potential field effects only. Compared to case 2, the mass-flow-averaged total pressure loss coefficient of the  $k-\epsilon$  simulation is 2.7% lower for case 3. Reduced losses might be expected with a favorable pressure gradient [44], but the result is inconclusive

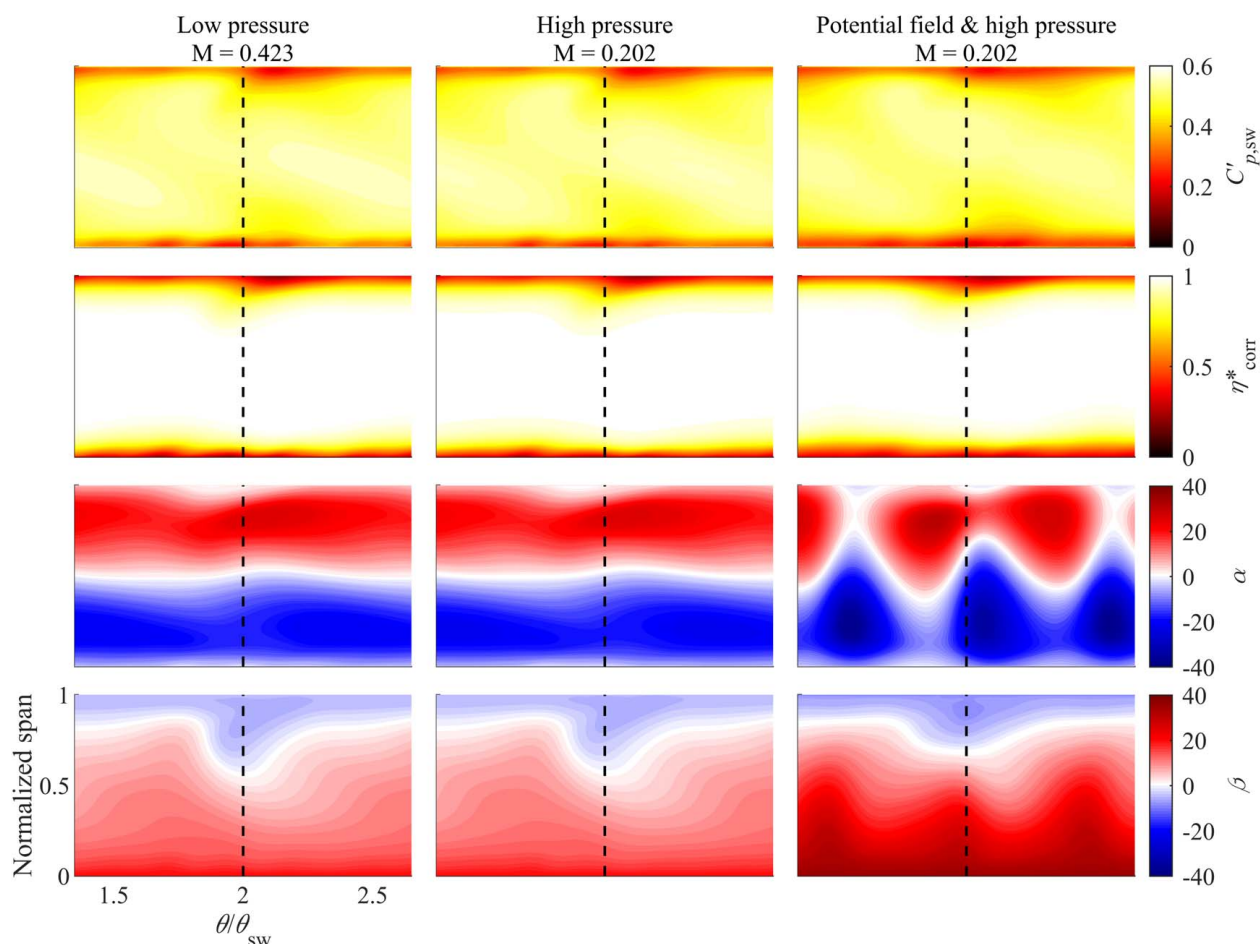


**Fig. 11 Comparison of CFD predictions with the  $k-\varepsilon$  model of the modified loss coefficient,  $C'_{p,sw}$ , corrected equivalent effectiveness,  $\eta^*_{corr}$ , swirl angle,  $\alpha$ , and pitch angle,  $\beta$ , at the reporting plane (viewed from upstream) for three simulations: (left) low exit pressure; (middle) high exit pressure; (right) high exit pressure with potential field caused by vanes. Dashed lines indicate swirler centerlines.**

noting variability in loss prediction depending on the grid refinement level.

The second row of Fig. 11 shows the non-dimensional total temperature (or effectiveness),  $T_{0,eff}$ . Whilst the distribution is virtually identical for cases 1 and 2, the prediction for the third case exhibits enhanced coolant penetration at the hub, which is thought to be associated with the differing annulus line. This is also reflected by the corresponding loss profile for the case with NGVs, which—due to coolant penetration—features a slightly thicker high total pressure region toward the hub.

The third and fourth rows of Fig. 11 show the swirl angle,  $\alpha$ , and pitch angle,  $\beta$ , respectively. The flow angles seem unaffected by the Mach number difference, with nearly identical distribution of swirl and pitch angle for cases 1 and 2.

When considering the case with NGVs (column 3), it is evident that the potential field dominates the flow angles at the reporting plane. Features are periodic in accordance with the vane locations, not those of the swirlers. Relative to the case with low back-pressure, the area-averaged swirl angle is lower by 2.5 deg. This leads to increases of the same magnitude in the incidence angle to the NGVs (see swirl angle sign convention in Fig. 1).

Turning our attention to the pitch angle (bottom row), a slight deviation from the cases without vanes arises due to two distinct effects. First, the annulus downstream of the reporting plane differs between the two domains, contracting further for the case with vanes (see annuli comparison in Fig. 4). Even though the flow path up to the reporting plane is almost identical, the potential field of the contracting NGV end walls cause the pitch angle to respond upstream. The second effect is the potential field of the

vane airfoils, generating circumferentially periodic heterogeneities of the pitch angle. These are however less prominent than the azimuthal variations witnessed for the swirl angle, as already noted in a similar study [24].

### Circumferential Flow Migration

Clocking of NGVs relative to the swirlers has previously been shown to affect the heat transfer and aerodynamic performance under lean-burn stage inlet conditions [2]. In designs with an integer NGV-to-swirler count ratio, the question of optimum circumferential clocking position arises. Here, the definition of circumferential position must be carefully considered, however, as there are two mechanisms by which circumferential migration of the vortex center between the swirler exit and the reporting plane can occur, leading to a difference between the geometric and effective positions. The first is the well-known potential field migration effect [24]. The second is due to net circulation around the machine axis due to net vorticity of the flow. Each effect is now briefly described.

The *potential field effect* is—simplistically—the migration of the vortex along the streamline pattern set up by the NGVs, though of course in any sophisticated analysis there is some degree of interaction of the two potential fields. In Ref. [24], this effect is described for the leading edge and passage-aligned clocking configurations. This effect is also shown in the simulations of Fig. 11: for the case with the vane potential field (right column), there is a

significant reduction in average swirl angle, resulting in increased incidence to the vanes.

The migration effect associated with *net-circulation* appears not to have been discussed in the literature. Here, we refer to net circulation around the machine axis (i.e., non-zero mass-average circumferential velocity) resulting from the net angular momentum of the field of individual vortices. As the vortices mix out (intra-vortex free shear or vortex–vortex interactions), this can lead to migration around the annulus. There are three contributing mechanisms for this effect, which we develop arguments for in Appendix B: effect of net-circulation on flow migration.

Exaggerated trends of the anticipated trajectories resulting from the potential field effect in isolation, as well as in superposition with net circulation, are illustrated in Fig. 1(b).

## Numerical Study on Circumferential Flow Migration

In experimental data, the vortex migration effect can only be inferred from the flowfield at the reporting plane: the circumferential location of the loss peak and the deformation of the thermal wake, for example, which are offset from the swirler centerline by 3–4 deg (CCW VFU). In CFD, however, the location of maximum pressure loss does not always coincide with other vortex identification criteria such as the Q-criterion, or the peak turbulence intensity. To provide insight into the relationship between these identification criteria, and the likely flow migration in practice, the circulation effect was investigated using CFD by calculating the mean circumferential flow migration between the settling plenum and the reporting plane from a parameter we call the *bulk yaw angle*,  $\alpha_{\text{bulk}}$ . We define  $\alpha_{\text{bulk}}$  as the ratio of the mass flow averages of the circumferential and the axial velocities (as opposed to the mass average of the yaw angle, which is not conservative)

$$\alpha_{\text{bulk}} = \arctan\left(\frac{\int \rho V_x V_\theta dA}{\int \rho V_x V_x dA}\right) \quad (11)$$

where  $\rho$  is the fluid density,  $V_x$  the axial velocity, and  $V_\theta$  the circumferential velocity (both in the machine reference frame). The integral is performed over a plane  $dA$  with an axial normal direction. The circumferential migration between two axial planes can then be calculated by integration:

$$\Delta\theta(x) = \int_{x_1}^{x_2} \left[ \frac{\tan(\alpha_{\text{bulk}})}{r_{\text{ref}}} \right] dx \quad (12)$$

where  $\Delta\theta$  is the cumulative change in circumferential machine coordinate,  $x_1$  and  $x_2$  are the axial coordinates of the planes,  $r_{\text{ref}}$  is a constant reference radius (equal to 360 mm), and  $\alpha_{\text{bulk}}$  is the bulk yaw angle. The term in square brackets is recalculated at each sampling plane. The expression can be discretized as required.

Figure 12 shows the circumferential migration,  $\Delta\theta$ , as a function of the axial coordinate, relative to the NGV leading edge (at  $x/C_{\text{ax}} = 0$ ) for the CFD simulations with the  $k-\varepsilon$  turbulence model (best similarity to experimental results). Results are shown for the three test cases in Table 3. An additional test case was performed with the diffuser removed to investigate its impact on flow migration.

Positive values represent migration in the counterclockwise (CCW) direction when viewed from upstream (VFU). For all cases with a diffuser, a positive bulk yaw angle (positive gradient of  $\Delta\theta$ ) initially develops in the swirler passages ( $x/C_{\text{ax}}$  between  $-11$  and  $-10$ ; Fig. 12), where free-shear dissipation within each vortex contributes to net circulation. Surprisingly, the expected direction of migration persists only until approximately midway through the diffuser passage (approximately  $x/C_{\text{ax}} \approx -9$ ; see Fig. 12), where the bulk circumferential flow direction changes from CCW VFU to clockwise (CW) VFU. This behavior is explained by a net negative circumferential pressure gradient (i.e., pressure tending from positive to negative in the CW VFU direction) that develops within the diffuser. The origin of this is not

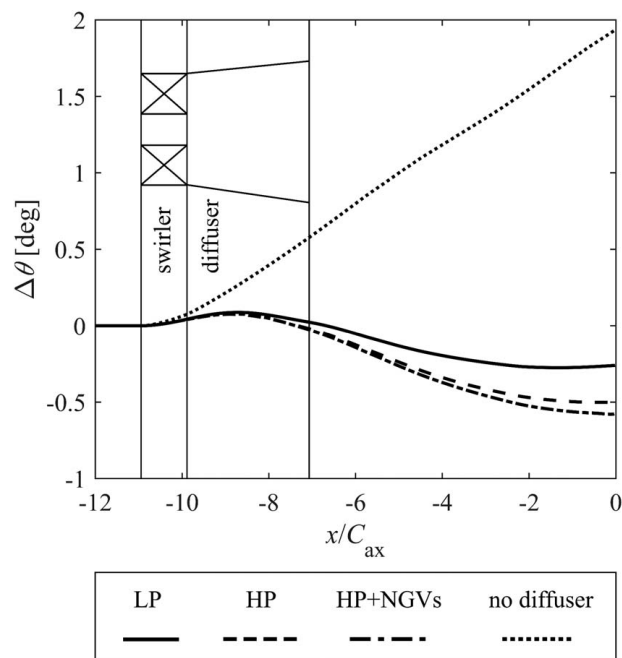


**Fig. 12 Circumferential flow migration calculated from integral of bulk yaw angle ( $\alpha_{\text{bulk}}$ ) for the  $k-\varepsilon$  turbulence model for low back-pressure; high back-pressure; NGV test case (with high back-pressure); no diffuser**

clear, but it appears to be associated with an asymmetric interaction of the vortex with the left-hand and right-hand radial walls of the diffuser, following the initial migration of the vortex core. What is surprising is that the vortex is turned from CCW VFU, through a stationary point, to CW VFU. This could be explained by the potential field being primarily developed in the higher Mach number upstream region, but persisting even into the lower Mach number downstream region (the result of diffusion), where the flow has the ability to be overturned as a result of its lower axial momentum. We coin the term “vortex reflection” to describe this behavior. Once the flow exits the diffuser, the vortex–vortex and intra-vortex free shear appear to result in transfer of individual vortex angular momentum to net circulation around the annulus. This results in a monotonic increase in  $\alpha_{\text{bulk}}$  for  $x/C_{\text{ax}} > -7$ , which results in an increase in the gradient of  $\Delta\theta$ , ultimately resulting in net circulation reversal between  $x/C_{\text{ax}} = -4$  and  $-1$ , depending on the test case.

Under low exit pressure conditions, the net circumferential flow migration at the reporting plane ( $x/C_{\text{ax}} = -0.5$ ) was approximately  $-0.25$  deg, i.e., mild migration in the opposite sense of rotation of the swirlers. For the high back-pressure case, CFD predicts  $-0.50$  deg. This result is approximately the same with and without NGVs, suggesting the vortex migration effect is relatively insensitive to the vane potential field. The swirler Mach number appears to have a mild influence on the net migration.

To understand the influence of the diffuser, an additional low back-pressure CFD case was run with the diffuser removed (using  $k-\varepsilon$ ). This is marked as the *no diffuser* case in Fig. 12. Immediately upon entering the swirler ( $x/C_{\text{ax}} = -11$ ), the flow begins to migrate CCW VFU. An approximately linear CCW trend develops downstream of the swirler, which persists up to the reporting plane and the vane leading edge. Minor inflections in the  $\Delta\theta$  trend are caused by the introduction of coolant jets, which cause blockage and an increase in the mean axial flow velocity, both of which decrease the bulk yaw angle. Without the diffuser, the net circumferential migration at the reporting plane was  $2.0$  deg CCW VFU, which is equivalent to approximately  $0.22$  NGV pitch spacings. These values are very large in comparison to the cases with



diffusers, highlighting the importance of performing simulations with realistic geometry when designing combustor simulators.

Net circumferential flow migration as a measure of vortex migration has the advantage of being a robustly defined parameter (Eq. (12)) that can be computed at every axial plane. This allows comparisons of migration trends of the form shown in Fig. 12. It is worth noting, however, that there are other measures of flow migration (e.g., the location of peak Q-criterion, peak turbulence intensity, or minimum total pressure) and all of these give slightly different measures of the vortex center location, and therefore the vortex migration. These inconsistencies highlight the complexity of uniquely defining the vortex center.

## Conclusions and Recommendations

The design and experimental commissioning of a fully annular lean-burn combustor simulator for the Engine Component Aero-thermal Testing Facility at the University of Oxford has been presented. The facility is an engine-parts cascade used for aero-thermal performance analysis of fully cooled nozzle guide vanes, and the combustor simulator allows studies of combustor-turbine interaction effects on NGV capacity and aero-thermal performance.

The combustor simulator has been characterized by measuring exit flow profiles of total pressure, total temperature, swirl angle, and pitch angle. The measurements were performed by removing the NGVs and traversing a four-swirler sector (72 deg) from downstream. To validate CFD design methods, and provide further insight into the flow mechanisms, complementary CFD studies were performed using  $k-\epsilon$ ,  $k-\omega$  SST, and SSG RSM turbulence models. The general flow profiles at the reporting plane were well-predicted by all methods. The best agreement in absolute total pressure loss and in coolant stream mixing and swirl profiles was achieved with the  $k-\epsilon$  model. We recommend this model for future design of similar systems. The SSG RSM model was found to underpredict mixing, compared to experiments, resulting in a different vortex structure at the reporting plane: we conclude that this method is probably unsuitable for design work.

The impact of acquiring profiles without vanes installed was assessed in CFD studies with and without vanes. Changes in back-pressure alone were found to have a negligible impact on the flow, but—as expected—the introduction of the vane potential field caused the area-averaged yaw angle to increase by approximately 2.5 deg at the reporting plane (located 0.5 NGV axial chords upstream of the NGV leading edge).

To understand design for particular clocking orientations, we study the flow migration effect in some detail. Two effects have been discussed, which include the vane potential field effect and a net-circulation effect. The first of these effects (vane potential field) was shown to cause a local increase in NGV incidence angles, without significantly impacting circumferential flow migration. The second effect (net circulation) has not been discussed in the literature but results in circumferential flow migration of 0.22 NGV pitches in the absence of a diffuser. For the ECAT CS, the net-circulation effect is largely suppressed by the diffuser, but this is thought to be highly geometry specific. The importance of accurate CFD design simulations with realistic geometry is emphasized by this study.

Both the experiments and simulations suggest that the ECAT combustor simulator achieves a lean-burn-representative temperature distortion and swirl intensity at the NGV inlet plane. The new module will be used for investigating the impact of lean-burn combustion profiles on NGV mass flow (capacity), overall effectiveness, and aerodynamic performance.

## Acknowledgment

The financial support of Rolls Royce plc and SILOET II under the Aerospace Technology Institute is gratefully acknowledged.

## Conflict of Interest

There are no conflicts of interest.

## Data Availability Statement

The authors attest that all data for this study are included in the paper.

## Nomenclature

### Roman Symbols

$C_{p,sw}$	= pressure loss coefficient (–)
$D$	= diameter (m)
$k_{corr}$	= effectiveness correction factor (–)
$\dot{m}$	= mass flow rate ( $\text{kg s}^{-1}$ )
$M$	= Mach number (–)
$p$	= pressure (total or static) (Pa)
$q$	= dynamic pressure (Pa)
$Re$	= Reynolds number (–)
$r$	= radius (m)
$R$	= gas constant of air ( $\text{J kg}^{-1} \text{K}^{-1}$ )
$S$	= swirl number (–)
$t$	= time (s)
$T$	= temperature (total or static) (K)
$V$	= velocity magnitude ( $\text{m s}^{-1}$ )
$V_r$	= radial velocity ( $\text{m s}^{-1}$ )
$V_x$	= axial velocity ( $\text{m s}^{-1}$ )
$V_\theta$	= circumferential velocity ( $\text{m s}^{-1}$ )
$x$	= axial coordinate (m)
$y^+$	= normalized wall distance (–)

### Greek Symbols

$\alpha$	= swirl angle (deg)
$\beta$	= pitch angle (deg)
$\gamma$	= ratio of specific heats (–)
$\delta_i$	= temporal offset (s)
$\eta^*$	= experimental effectiveness (–)
$\eta_{corr}^*$	= corrected experimental effectiveness (–)
$\theta$	= circumferential location (deg)
$\mu$	= dynamic viscosity ( $\text{Pa s}$ )
$\rho$	= density ( $\text{kg m}^{-3}$ )
$\sigma$	= standard error variable

### Subscripts

0	= total condition
1	= quantity measured at plane 1
2	= quantity measured at plane 2
3	= quantity measured at plane 3
c	= cold-stream inlet
exit	= vane exit
h	= hot-stream inlet
m	= mainstream
sw	= swirler property

## Appendix A: Grid Sensitivity Study

In this section, we consider the sensitivity of the numerical results to the resolution of the computational grid.

**Refinement Strategy and Test Cases.** The grids with and without vanes were both refined by successively decreasing cell sizes globally. In the combustor simulator, cell sizes (based on approximate edge length) were decreased from 0.80 mm to 0.60 mm to 0.48 mm, resulting in cell counts of 20, 39, and 67 million (respectively) for the case *without* vanes. Corresponding grid sizes for the case *with* vanes were 27, 52, and 87 million

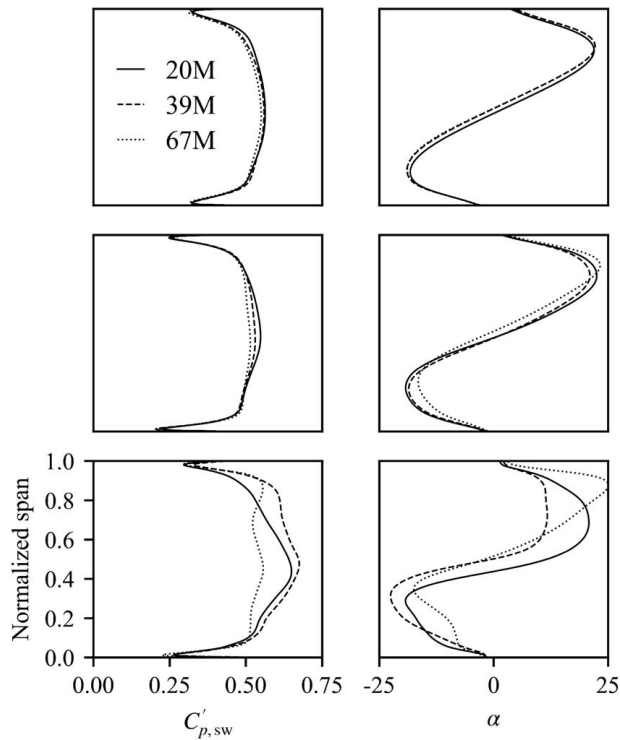


**Fig. 13** Grid sensitivity of the loss coefficient,  $C'_{p,sw}$ , and the swirl angle,  $\alpha$ , at the reporting plane for the low-pressure case using the  $k-\epsilon$ ,  $k-\omega$  SST, and SSG RSM models

For the low-pressure case, grid sensitivity was studied for the  $k-\epsilon$ ,  $k-\omega$  SST, and SSG RSM turbulence models. The grid sensitivity study for the case with NGVs was completed for the  $k-\epsilon$  model only.

**Low-Pressure Case Grid Sensitivity.** Variables of interest are the swirl/pitch angle distribution, loss coefficient, and temperature profile at the reporting plane. Our preliminary analysis showed that temperature and pitch angle were relatively insensitive to mesh refinement. We therefore report only the—more critical—loss and swirl angle distributions. Reporting plane profiles of the loss coefficient (Eq. (10)) and the swirl angle (Eq. (7)) are shown in Fig. 13 for the  $k-\epsilon$ ,  $k-\omega$  SST, and SSG RSM models.

For  $k-\epsilon$ , some grid sensitivity of the loss coefficient can be seen, with mass-flux-averaged loss ranging between 0.497 (20 M cells) and 0.485 (67 M cells). For the swirl angle, the first refinement step (20 M  $\rightarrow$  39 M) caused the vortex to move radially downward, whereas the profiles for the intermediate (39 M) and most refined mesh (67 M) are essentially identical. This suggests that the intermediate and most refined grids are adequate for  $k-\epsilon$ .

For  $k-\omega$  SST, mass-flux-averaged loss varies between 0.463 (67 M) and 0.468 (20 M). The radial profiles of the loss coefficient

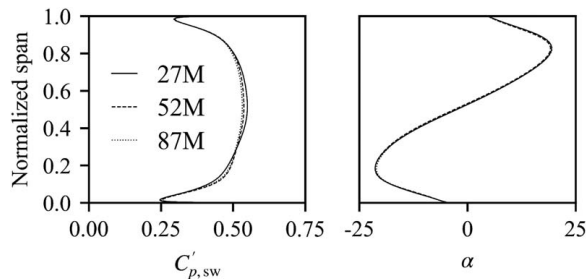


**Fig. 14** Grid sensitivity study of the loss coefficient,  $C'_{p,sw}$ , and the swirl angle,  $\alpha$ , at the reporting plane for the case with NGVs using the  $k-\epsilon$  turbulence model

are generally similar, with a gradual reduction in loss around midspan as the mesh is refined. Area-averaged  $y^+$  values range between 1.52 (20 M) and 0.93 (67 M) with a maximum of around 6.6 for all three cases. Despite the relatively high degree of mesh refinement, the swirl angle profile does not appear to be fully grid independent, with differences of approximately 1 deg for the maximum and minimum swirl angles between subsequent refinement steps.

For SSG RSM, both the loss and swirl profiles changed significantly between both refinement steps. Mass-flux-averaged loss changed from 0.535 (20 M) to 0.499 (67 M cells). Swirl angle extrema changed by as much as 5 deg.

Overall, the grid sensitivity study shows that even for relatively fine grids, neither  $k-\omega$  SST or SSG RSM achieve the same degree of grid independence as the  $k-\epsilon$  model. This demonstrates the challenges of simulating this type of flow.

**Case with Vanes Grid Sensitivity.** Reporting plane profiles of loss coefficient and swirl angle for the case with vanes using  $k-\epsilon$  are shown in Fig. 14. The mass-flux-averaged loss coefficient ranges between 0.470 (27 M) and 0.466 (87 M). The swirl angle profiles are effectively identical, with all three solutions falling within 0.5 deg of each other.

## Appendix B: Effect of Net-Circulation on Flow Migration

In this section, we consider the impact of net circulation on circumferential flow migration. This effect appears to not have been discussed in the literature.

**Effect 1: Conservation of Angular Momentum About Machine Axis.** Imagine an annulus with  $N$  discrete swirlers, A, B, C, ..., N, as shown in Fig. 15. We argue as follows:

- (1) Swirler applies a torque on the flow giving rise to net angular momentum both about the individual swirler axes A, B, C, etc. and—as a consequence—about the machine axis  $x$ .
- (2) If the vortices suffer no internal (free shear) or external (wall) shear, and noting there is net angular momentum about the machine axis, it is possible for the vortices to persist indefinitely along an axial path  $S_1$ .
- (3) As the vortices interact and mix out, the angular momentum terms associated with individual decaying vortex cores (A, B, C, etc.) reduce (no local conservation required). The angular momentum about the machine axis must be conserved. As individual vortices decay the entire flow must therefore start to rotate about the machine axis. The mean flow therefore follows trajectory  $S_2$ , not  $S_1$ .

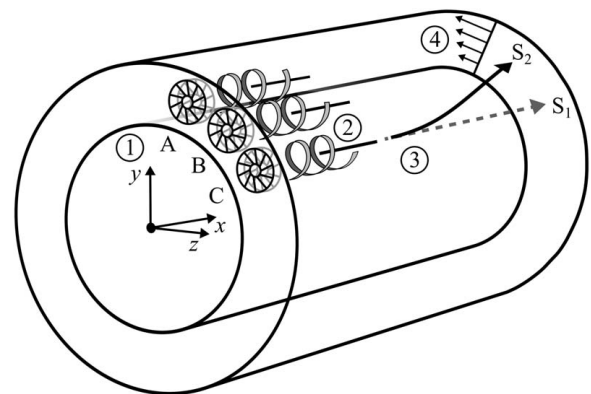


**Fig. 15** Net migration due to the conservation of angular momentum alone

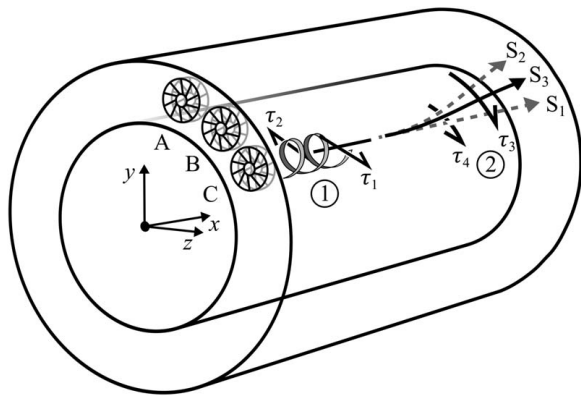


Fig. 16 Influence of wall shear on net migration

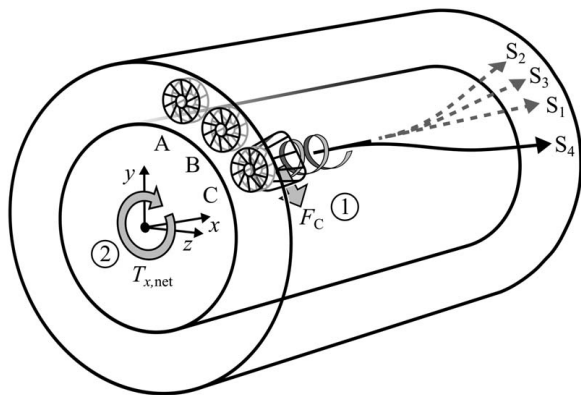


Fig. 17 Effect of diffuser on net migration

- (4) In the absence of external shear and pressure, the flow initially mixes out such that it satisfies the convention of angular momentum about  $x$  and radial equilibrium.

**Effect 2: External Shear.** Now, consider the same problem but with wall shear forces acting on the vortices, as shown in Fig. 16. We argue as follows:

- (1) During the decay process, external shear (hub and case walls) acts both with ( $\tau_2$ ) and against ( $\tau_1$ ) the direction of net rotation. The direction (+ or -) of this secondary influence on net migration is ambiguous.
- (2) In the “initially mixed” state, the external shear forces  $\tau_3$  and  $\tau_4$  both act to oppose the net migration. The secondary influence of external shear is to reduce net migration. The path is changed from  $S_2$  to  $S_3$ .

**Effect 3: Pressure Distribution in Diffuser.** Finally, consider an effect associated with the swirler diffuser (if present), the geometry for which is illustrated in Fig. 17. We argue as follows:

- (1) If the swirler is provided with a diffuser, the interaction of the individual vortices with their respective diffuser walls will, in general, give rise to pressure thrust terms  $F_A$ ,  $F_B$ , and  $F_C$ , etc.
- (2) Circular symmetry implies that the net force (entire annulus) in the  $z-y$  plane (see diagram) on the entire flow is zero, but in general there could be a net axial thrust  $F_x$  and a net torque about the machine axis,  $T_{x,net}$ . This may result in a full reversal of the general trend described under effects 1 and 2, changing the trajectory from  $S_3$  to  $S_4$ .

## References

- [1] Shang, T., and Epstein, A. H., 1997, “Analysis of Hot Streak Effects on Turbine Rotor Heat Load,” *ASME J. Turbomach.*, **119**(3), pp. 544–553.

- [2] Khanal, B., He, L., Northall, J., and Adami, P., 2013, “Analysis of Radial Migration of Hot-Streak in Swirling Flow Through High-Pressure Turbine Stage,” *ASME J. Turbomach.*, **135**(4), p. 041005.
- [3] Lubbock, R. J., and Oldfield, M. L. G., 2018, “Turbulent Velocity and Pressure Fluctuations in Gas Turbine Combustor Exit Flows,” *Proc. Inst. Mech. Eng. Part A J. Power Energy*, **232**(4), pp. 337–349.
- [4] Povey, T., and Qureshi, I., 2009, “Developments in Hot-Streak Simulators for Turbine Testing,” *ASME J. Turbomach.*, **131**(3), p. 031009.
- [5] Kirolos, B., Lubbock, R., Beard, P. F., Goenaga, F., Rawlinson, A., Janke, E., and Povey, T., 2017, “ECAT: an Engine Component Aerothermal Facility at the University of Oxford,” *ASME Turbo Expo 2017 (Turbomachinery Technical Conference and Exposition)*, Charlotte, NC, June 26–30, Paper No. GT2017-64736.
- [6] Barringer, M., Thole, K. A., and Polanka, M. D., 2004, “Developing a Combustor Simulator for Investigating High Pressure Turbine Aerodynamics and Heat Transfer,” *ASME Turbo Expo 2004 (Power for Land, Sea, and Air)*, Vienna, Austria, June 14–17, pp. 565–575, Paper No. GT2004-53613.
- [7] Cresci, I., Ireland, P. T., Bacic, M., Tibbott, I., and Rawlinson, A., 2015, “Realistic Velocity and Turbulence Intensity Profiles at the Combustor-Turbine Interaction (CTI) Plane in a Nozzle Guide Vane Test Facility,” *Proceedings of the 11th European Conference on Turbomachinery Fluid Dynamics & Thermodynamics*, Madrid, Spain, Mar. 23–27, Paper No. ETC2015-255.
- [8] Qureshi, I., and Povey, T., 2011, “A Combustor-Representative Swirl Simulator for a Transonic Turbine Research Facility,” *Proc. Inst. Mech. Eng. Part G J. Aerosp. Eng.*, **225**(7), pp. 737–748.
- [9] Beard, P. F., Smith, A. D., and Povey, T., 2014, “Effect of Combustor Swirl on Transonic High Pressure Turbine Efficiency,” *ASME J. Turbomach.*, **136**(1), p. 011002.
- [10] Qureshi, I., Beretta, A., Chana, K. S., and Povey, T., 2012, “Effect of Aggressive Inlet Swirl on Heat Transfer and Aerodynamics in an Unshrouded Transonic HP Turbine,” *ASME J. Turbomach.*, **134**(6), p. 061023.
- [11] Duchaine, F., Dombard, J., Gicquel, L., and Koupper, C., 2017, “Integrated Large Eddy Simulation of Combustor and Turbine,” *Proceedings of the ASME Turbo Expo 2017 (Turbomachinery Technical Conference and Exposition)*, Charlotte, NC, June 26–30, Paper No. GT2017-63473.
- [12] Rehder, H.-J., Pahs, A., Bittner, M., and Kocian, F., 2017, “Next Generation Turbine Testing at DLR,” *ASME Turbo Expo. (Power for Land, Sea, and Air)*, Charlotte, NC, June 26–30, Paper No. GT2017-64409.
- [13] Krumme, A., Tegeler, M., and Gattermann, S., 2019, “Design, Integration and Operation of a Rotating Combustor-Turbine-Interaction Test Rig Within the Scope of EC FP7 Project FACTOR,” *Proceedings of the 13th European Conference on Turbomachinery Fluid Dynamics & Thermodynamics*, Lausanne, Switzerland, Apr. 8–12, Paper No. ETC2019-035.
- [14] Koupper, C., Cacioli, G., Gicquel, L., Duchaine, F., Bonneau, G., Tarchi, L., and Facchini, B., 2014, “Development of an Engine Representative Combustor Simulator Dedicated to Hot Streak Generation,” *ASME J. Turbomach.*, **136**(11), p. 111007.
- [15] Bacci, T., Cacioli, G., Facchini, B., Tarchi, L., Koupper, C., and Champion, J.-L., 2015, “Flowfield and Temperature Profiles Measurements on a Combustor Simulator Dedicated to Hot Streaks Generation,” *ASME Turbo Expo 2015 (Turbine Technical Conference and Exposition)*, Montreal, PQ, Canada, June 15–19, Paper No. GT2015-42217.
- [16] Bacci, T., Facchini, B., Picchi, A., Tarchi, L., Koupper, C., and Champion, J.-L., 2015, “Turbulence Field Measurements at the Exit of a Combustor Simulator Dedicated to Hot Streaks Generation,” *ASME Turbo Expo 2015 (Turbine Technical Conference and Exposition)*, Montreal, PQ, Canada, June 15–19, Paper No. GT2015-42218.
- [17] Hall, B. F., Chana, K. S., and Povey, T., 2014, “Design of a Nonreacting Combustor Simulator With Swirl and Temperature Distortion With Experimental Validation,” *ASME J. Eng. Gas Turbines Power*, **136**(8), p. 081501.
- [18] Terhaar, S., Oberleithner, K., and Paschereit, C. O., 2015, “Key Parameters Governing the Precessing Vortex Core in Reacting Flows: An Experimental and Analytical Study,” *Proc. Combust. Inst.*, **35**(3), pp. 3347–3354.
- [19] Oberleithner, K., Terhaar, S., Rukes, L., and Paschereit, C. O., 2013, “Why Non-Uniform Density Suppresses the Precessing Vortex Core,” *ASME J. Eng. Gas Turbines Power*, **135**(12), p. 121506.
- [20] Hall, B. F., and Povey, T., 2015, “Experimental Study of a Non-reacting Low NOx Combustor Simulator for Scaled Turbine Experiments,” *ASME Turbo Expo 2015 (Turbine Technical Conference and Exposition)*, Montreal, PQ, Canada, June 15–19, Paper No. GT2015-43530.
- [21] Adams, M. G., Povey, T., Hall, B. F., Cardwell, D. N., Chana, K. S., and Beard, P. F., 2020, “Commissioning of a Combined Hot-Streak and Swirl Profile Generator in a Transonic Turbine Test Facility,” *ASME J. Eng. Gas Turbines Power*, **142**(3), p. 031008.
- [22] Adams, M. G., Beard, P. F., Stokes, M. R., Wallin, F., Chana, K. S., and Povey, T., 2021, “Effect of a Combined Hot Streak and Swirl Profile on Cooled 1.5-Stage Turbine Aerodynamics: an Experimental and Computational Study,” *ASME J. Turbomach.*, **143**(2), p. 021011.
- [23] Koupper, C., Gicquel, L., Duchaine, F., Bacci, T., Facchini, B., Picchi, A., Tarchi, L., and Bonneau, G., 2016, “Experimental and Numerical Calculation of Turbulent Timescales at the Exit of an Engine Representative Combustor Simulator,” *ASME J. Eng. Gas Turbines Power*, **138**(2), p. 021503.
- [24] Koupper, C., Bonneau, G., Gicquel, L., and Duchaine, F., 2016, “Large Eddy Simulations of the Combustor Turbine Interface: Study of the Potential and Clocking Effects,” *ASME Turbo Expo 2016 (Turbomachinery Technical Conference and Exposition)*, Seoul, South Korea, June 13–17, Paper No. GT2016-56443.



- [25] Bacci, T., Becchi, R., Picchi, A., and Facchini, B., 2019, "Adiabatic Effectiveness on High-Pressure Turbine Nozzle Guide Vanes Under Realistic Swirling Conditions," *ASME J. Turbomach.*, **141**(1), p. 011009.
- [26] Bacci, T., Lenzi, T., Picchi, A., Mazzei, L., and Facchini, B., 2019, "Flow Field and Hot Streak Migration Through High Pressure Cooled Vanes With Representative Lean Burn Combustor Outflow," *ASME J. Eng. Gas Turbines Power*, **141**(4), p. 041020.
- [27] Bacci, T., Picchi, A., Lenzi, T., and Facchini, B., 2019, "Turbulence Intensity Measurements Across a NGV Cooled Cascade With Representative Lean Burn Combustor Outflow," Proceedings of the 13th European Conference on Turbomachinery Fluid Dynamics & Thermodynamics, Lausanne, Switzerland, Apr. 8–12, Paper No. ETC2019-100.
- [28] Messenger, A., and Povey, T., 2020, "Calibrated Low-Order Transient Thermal and Flow Models for Robust Test Facility Design," *J. Glob. Power Propuls. Soc.*, **4**, pp. 94–113.
- [29] Shahpar, S., and Caloni, S., 2013, "Aerodynamic Optimization of High-Pressure Turbines for Lean-Burn Combustion System," *ASME J. Eng. Gas Turbines Power*, **135**(5), p. 055001.
- [30] Povey, T., and Qureshi, I., 2008, "A Hot-Streak (Combustor) Simulator Suited to Aerodynamic Performance Measurements," *Proc. Inst. Mech. Eng. Part G J. Aerosp. Eng.*, **222**(6), pp. 705–720.
- [31] Chaluvasi, V. S. P., Kalfas, A. I., Baniaghbal, M. R., Hodson, H. P., and Denton, J. D., 2001, "Blade-Row Interaction in a High-Pressure Turbine," *J. Propul. Power*, **17**(4), pp. 892–901.
- [32] Kilik, E., 1976, "The Influence of Swirler Design Parameters on the Aerodynamics of Downstream Recirculation Region," Ph.D. thesis, Cranfield University, Cranfield.
- [33] Chigier, N. A., and Beér, J. M., 1964, "Velocity and Static-Pressure Distributions in Swirling Air Jets Issuing From Annular and Divergent Nozzles," *ASME J. Fluids Eng.*, **86**(4), pp. 788–796.
- [34] Lucca-Negro, O., and O'Doherty, T., 2001, "Vortex Breakdown: A Review," *Prog. Energy Combust. Sci.*, **27**(4), pp. 431–481.
- [35] Burdett, D., Goenaga, F., and Povey, T., 2021, "Understanding Capacity Sensitivity of Cooled Transonic Nozzle Guide Vanes: A Parametric Experimental and Computational Study of the Impact of Trailing Edge Geometry," *ASME J. Turbomach.*, **143**(5), p. 051001.
- [36] Michaud, M., Jackson, D., Goenaga, F., and Povey, T., 2022, "Experimental Study of Impact of In-service Deterioration on Aerodynamic Performance of High-Pressure Nozzle Guide Vanes," *ASME J. Turbomach.*, Paper No. TURBO-21-1259 (in review)
- [37] Burdett, D., Lubbock, R. J., and Povey, T., 2018, "An Impulse Response Technique to Improve the Effective Frequency Response of Pressure Probes," Proceedings of the 24th Symposium on Measuring Techniques in Turbomachinery (Transonic and Supersonic Flow in Cascades and Turbomachines), Prague, Czech Republic, Aug. 30–31, Paper No. MTT2418B23.
- [38] Paniagua, G., Dénos, R., and Oropesa, M., 2002, "Thermocouple Probes for Accurate Temperature Measurements in Short Duration Facilities," ASME Turbo Expo 2002 (Power for Land, Sea, and Air), Amsterdam, The Netherlands, June 3–6, Paper No. GT2002-30043.
- [39] Carslaw, H. S., and Jaeger, J. C., 1959, *Conduction of Heat in Solids*, 2nd ed., Oxford University Press, London.
- [40] Wilcox, D.C., 2006. *Turbulence Modeling for CFD*, 3rd ed., DCW Industries, La Cañada, CA.
- [41] Menter, F. R., 1994, "Two-Equation Eddy-Viscosity Turbulence Models for Engineering Applications," *AIAA J.*, **32**(8), pp. 1598–1605.
- [42] Speziale, C. G., Sarkar, S., and Gatski, T. B., 1991, "Modelling the Pressure-Strain Correlation of Turbulence: An Invariant Dynamical Systems Approach," *J. Fluid Dyn.*, **227**, pp. 245–272.
- [43] Escue, A., and Cui, J., 2010, "Comparison of Turbulence Models in Simulating Swirling Pipe Flows," *Appl. Math. Model.*, **34**(10), pp. 2840–2849.
- [44] Denton, J. D., 1993, "Loss Mechanisms in Turbomachines," ASME 1993 International Gas Turbine and Aeroengine Congress and Exposition, Cincinnati, OH, May 24–27, Paper No. 93-GT-435.